Nanoscale

PAPER

View Article Online
View Journal | View Issue

Cite this: *Nanoscale*, 2020, **12**, 16917

Inkjet-defined site-selective (IDSS) growth for controllable production of in-plane and out-of-plane MoS_2 device arrays†

Byunghoon Ryu, *‡ Jeong Seop Yoon, ‡ Eric Kazyak, Kuan-Hung Chen, Younggeun Park, Neil P. Dasgupta and Xiaogan Liang*

Along with the increasing interest in MoS_2 as a promising electronic material, there is also an increasing demand for nanofabrication technologies that are compatible with this material and other relevant layered materials. In addition, the development of scalable nanofabrication approaches capable of directly producing MoS_2 device arrays is an imperative task to speed up the design and commercialize various functional MoS_2-based devices. The desired fabrication methods need to meet two critical requirements. First, they should minimize the involvement of resist-based lithography and plasma etching processes, which introduce unremovable contaminations to MoS_2 structures. Second, they should be able to produce MoS_2 structures with in-plane or out-of-plane edges in a controlled way, which is key to increase the usability of MoS_2 for various device applications. Here, we introduce an inkjet-defined site-selective (IDSS) method that meets these requirements. IDSS includes two main steps: (i) inkjet printing of micro-scale liquid droplets that define the designated sites for MoS_2 growth, and (ii) site-selective growth of MoS_2 at droplet-defined sites. Moreover, IDSS is capable of generating MoS_2 with different structures. Specifically, an IDSS process using deionized (DI) water droplets mainly produces in-plane MoS_2 features, whereas the processes using graphene ink droplets mainly produce out-of-plane MoS_2 features rich in exposed edges. Using out-of-plane MoS_2 structures, we have demonstrated the fabrication of miniaturized on-chip lithium ion batteries, which exhibit reversible lithiation/delithiation capacity. This IDSS method could be further expanded as a scalable and reliable nanomanufacturing method for generating miniaturized on-chip energy storage devices.

Received 26th May 2020,
Accepted 4th August 2020

DOI: 10.1039/d0nr04012f

rsc.li/nanoscale

1. Introduction

Although the exploding amount of research has touted the excellent properties of Molybdenum disulfide (MoS_2) and demonstrated its use as functional devices exhibiting interesting characteristics,[1–4] relatively few studies have been focusing on the top-down fabrication of reliable and ordered MoS_2 structures.[5,6] So far, the research society still highly relies on mechanical exfoliation and conventional chemical vapor deposition (CVD) methods to generate MoS_2 features. Such conventional methods, however, are only appropriate for the fundamental research in the lab-scale device demonstration and can hardly be considered as potential manufacturing solutions for production of orderly arranged MoS_2 structures. This is because neither mechanical exfoliation nor CVD can generate MoS_2 device features at designated locations. Furthermore, to produce ordered MoS_2 arrays that have in-plane or out-of-plane edges, conventional methods need to be modified by incorporating special growth schemes,[7] which increases the fabrication complexity and induces unpredictable contaminations. Such limitations of the conventional fabrication methods retard the practical device implementations of MoS_2, such as thin-film transistors (TFTs), multiplexing biosensors, and integrative energy storage components, which are based on specifically controlled in-plane or out-of-plane MoS_2 structures.

To address such a fabrication-oriented challenge, desired nanofabrication approaches need to be able to lithographically generate orderly arranged MoS_2 device structures with in-plane or out-of-plane edges. A viable approach should avoid any resist-based lithography or plasma-based etching processes. This is because of the fact that these processes bring about a

Department of Mechanical Engineering, University of Michigan, Ann Arbor, MI 48109, USA. E-mail: bhryu@umich.edu, xiaoganl@umich.edu

†Electronic supplementary information (ESI) available: EDS spectrum analysis on DI water residues (Fig. S1); transfer characteristic curves measured from the IDSS-produced 16 FETs (Fig. S2); Raman characterization of dispensed graphene flakes (Fig. S3); impedance plot of the on-chip battery electrode (Fig. S4). See DOI: 10.1039/d0nr04012f

‡These authors contributed equally to this work.

wide range of contaminants that complicatedly change or degrade electrical and electrochemical properties of MoS_2 structures. Such contaminants are much more detrimental to the properties of MoS_2 than to those of bulk materials because of the atomically layered structures of MoS_2 and other relevant 2D materials.[8–12] More seriously, state-of-the-art wafer cleaning techniques (*e.g.*, piranha and RCA methods) cannot clean up these process-introduced contaminants without accompanying serious chemical or physical damages to MoS_2 structures. Such a difficulty in sample cleaning is due to the fact that atomically layered MoS_2 structures, which are formed by van der Waals force, are vulnerable in such cleaning solutions, and also due to the fact that MoS_2 and other van der Waals solids with relatively inertial surfaces have a relatively weak bonding strength to the hosting wafer and are easily delaminated by the cavitation in a cleaning process.[13,14] Therefore, it is highly desirable to develop a scalable fabrication technique that avoids use of resist and plasma, capable of producing orderly arranged MoS_2 structures with in-plane or out-of-plane edges.

In this study, we develop an inkjet-defined site-selective growth (IDSS) method, which takes advantage of inkjet printing and CVD processes, capable of growing both in-plane and out-of-plane MoS_2 structures in a controllable fashion at deterministic locations on a chip substrate. An IDSS process mainly includes two steps: (i) inkjet dispensing of solution droplets (*e.g.*, deionized water (DI) or graphene ink) followed with drying of the droplets to predefine the target locations on a substrate for growing MoS_2 features, and (ii) site-selective CVD growth of in-plane or out-of-plane MoS_2 structures at the substrate locations, where droplets are inkjet-dispensed. Such a selective growth scheme in IDSS is attributed to the fact that dried solution droplets leave behind small amounts of residues (*e.g.*, impurities or graphene flakes), which could lead to local topography changes within droplet-covered regions and serve as effective nucleation seeds during the CVD process.[15,16] Importantly, in addition to enabling site-selective growth, IDSS can also be used to control the in-plane/out-of-plane orientation of the resulting MoS_2 structures.

Specifically, the composition of the ink determines the orientation. Using DI water droplets to define growth locations dominantly produces in-plane MoS_2 features. We have demonstrated fabrication of an array of the working transistors based on such in-plane MoS_2 features, which exhibit a good uniformity in their transfer characteristics. In contrast, using graphene ink droplets to define growth locations dominantly produces out-of-plane MoS_2 features selectively nucleated on top of inkjet-deposited graphene flakes. Such a hierarchical structure of out-of-plane MoS_2/graphene is rich in exposed edges and could serve as an efficient lithium-ion battery anode structure. This MoS_2 structure could provide high storage density of lithium ions, high charge/discharge rates (due to exposed edges), as well as small footprint size on a chip. Using IDSS-produced out-of-plane structures, we have demonstrated the fabrication of miniaturized lithium-ion batteries, with a footprint size of ~1 mm and good discharge/charge capacity parameters (206 μA h cm^{-2}/113 μA h cm^{-2} at 55 μA cm^{-2} current density).

2. Results and discussion

Fig. 1 illustrates the inkjet-defined site-selective growth (IDSS) method for growing an array of in-plane MoS_2 features on a target substrate. Following the sequence of processing steps, Fig. 1(a) schematically shows the inkjet printing step for dispensing an array of DI water droplets on the target substrate. The dispensed droplets predefine the locations, where MoS_2 features are to be nucleated in the subsequent steps. The inkjet printer used for this work can dispense a minimum droplet volume of ~10 pL, which typically deposits droplets on a SiO_2/Si substrate with an average footprint diameter of about tens of micrometers.[17] This inkjet printer can also print out droplet arrays with droplet-to-droplet spacings ranging from tens to hundreds of micrometers. As illustrated in Fig. 1(b), as-deposited droplets of DI water evaporate quickly on the target substrate. During the drying process, DI water droplets leave behind DI water residues on the substrate, which can serve as effective nucleation seeds for the subsequent CVD process.[15,18] Fig. 1(c) illustrates the site-selective CVD of MoS_2 features on the substrate, and Fig. 1(d) illustrates as-grown in-plane MoS_2 features. Specifically, in-plane MoS_2 features, whose crystal grains dominantly grow along the substrate surface, are synthesized at the spots covered by DI water droplets. More information about the IDSS process is presented in the Materials and methods section.

Fig. 2 shows a comparative study to reveal the scientific mechanism responsible for the site-selective growth capability of IDSS. Fig. 2(a) schematically illustrates the nucleation of MoS_2 during a regular CVD process without using IDSS. According to classical nucleation theory (CNT),[19] the nucleation rate of MoS_2 on the 2D substrate surface can be estimated by eqn (1),[20]

$$R_{\text{nucleation}} = R_0 e^{(-\Delta G/k_b T)} \quad (1)$$

where k_b and T are Boltzmann constant and absolute temperature, respectively. R_0 is a prefactor related to number of nucleation sites, time rate of precursor molecules attached to the

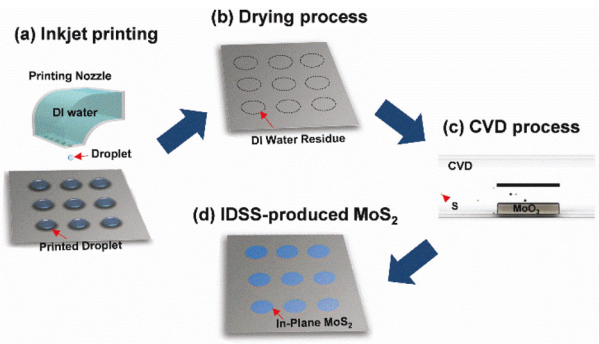

Fig. 1 Setup of the IDSS process: (a) schematic illustration of inkjet printing step for dispensing an array of DI water droplets on the dielectric substrate; (b) drying the droplet patterns before loading the sample into CVD quartz tube; (c) site-selective CVD growth of MoS_2 patterns; (d) IDSS-produced in-plane MoS_2 features.

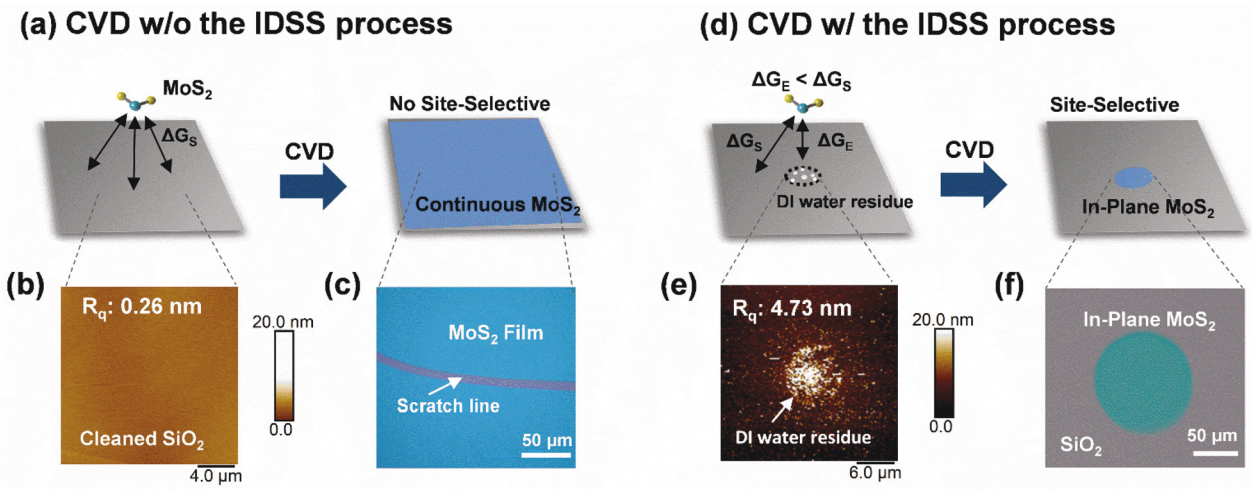

Fig. 2 Growth of in-plane MoS_2 structure with and without IDSS process: (a) schematic illustration of the conventional CVD without IDSS process, which leads to in-plane MoS_2 with no site-selective nucleation. (b) AFM image of cleaned SiO_2/Si substrate; (c) optical micrograph of CVD-grown continuous MoS_2 film; (d) schematic illustration of the site-selective nucleation of in-plane MoS_2 using IDSS process; (e) AFM image of a dry SiO_2/Si substrate area ever covered by an inkjet-dispensed DI water droplet; (f) optical micrograph of IDSS-produced in-plane MoS_2 pixel.

nucleus, and probability of the nucleus to form MoS_2. Finally, ΔG is the free energy required for MoS_2 nucleus to overcome the nucleation barrier (*i.e.*, nucleation barrier energy). Based on the eqn (1), the nucleation rate ($R_{nucleation}$) of MoS_2 on a flat SiO_2/Si substrate without involving IDSS is reasonably considered to be uniform throughout the whole target surface. This is because of the small size of the substrate (2 cm × 2 cm), which leads to uniform temperature and precursor concentration distributions over the whole surface. Furthermore, before CVD, the substrate is subjected to strong cleaning protocols (*e.g.*, RCA or Piranha), which can eliminate most adsorbates. Such a cleaned smooth surface of the substrate shows a homogeneous nucleation barrier energy distribution across the entire surface, which results in a continuous MoS_2 film without exhibiting any site-selective nucleation preference. Our experimental results support the aforementioned discussion. Fig. 2(b) shows the AFM topography image of a cleaned SiO_2/Si surface, which serves as a control substrate. The root mean squared surface roughness (R_q) of this control substrate is measured to be ~0.26 nm. After a CVD process, this cleaned substrate surface is covered by a continuous MoS_2 film, which does not show any spatial selectivity for MoS_2 nucleation, as shown in Fig. 2(c). On the other hand, the IDSS process can produce MoS_2 structures at selective sites. Schematic diagrams shown in Fig. 2(d) describe the hypothesized mechanism of the site-selective nucleation of MoS_2 by IDSS. In this case, we assume that the nucleation barrier energy is the only parameter affected by the IDSS process in eqn (1). The AFM image shown in Fig. 2(e) displays the surface topography of a dry SiO_2/Si substrate area ever covered by an inkjet-dispensed DI water droplet. The surface roughness (R_q) of this substrate area is measured to be ~4.73 nm that is about 20 times larger than that of the control substrate area or the surroundings. This indicates that even type 1 ASTM DI water droplets still contain minuscule residues that are deposited on the substrate after the drying of the dispensed droplets.[21] Furthermore, the formation of such residues could be attributed to one of the characteristics of DI water. Specifically, DI water tends to attract minerals and elements from its surroundings to thermodynamically compensate for its deficiency in ions.[22] Fig. S1† shows the energy-dispersive X-ray spectroscopy (EDS) analysis results on the DI water residues on an inkjet-processes substrate. Specifically, the SEM image in Fig. S1(a)† displays the DI-water-deposited residues on a SiO_2/Si substrate. In Fig. S1(a),† Arrows (1) and (2) denote the region with residues and the intact surface region outside of the residues, respectively. Fig. S1(b) and (c)† display the EDS spectra acquired from the locations denoted by Arrows (1) and (2), respectively. These two EDS spectra do not exhibit any noticeably different features. This observation implies that the residues likely result from the aggregation of the minerals already existing on the SiO_2/Si substrate. Such residues increase the surface roughness of the substrate areas ever covered by the droplets and form a lot of step edges within these regions. It has been reported that the nucleation barrier energy at a step edge (ΔG_E) is lower than at a smooth surface (ΔG_S), which brings about the fast and preferential nucleation of a nucleus at the step edge.[20,23] The computation results by Gao *et al.* show that for CVD growth of graphene, the nucleation barrier energy at a step edge is 1.0–2.0 eV lower than that at a smooth surface.[20] Therefore, it would be reasonable to hypothesize that the step edges generated by DI droplets are the key factor inducing the site-selective nucleation of MoS_2. The optical micrograph shown in Fig. 2(f) shows an in-plane MoS_2 pixel synthesized at a designated location by IDSS, which supports the hypothesis.

Generally, inkjet printing can dispense a broad variety of liquid solutions into various array patterns through the programming of the dispensing courses. By taking advantage of

such an ability of inkjet printing, the IDSS method can controllably produce various MoS_2 array patterns with no need of additional lithography and plasma processes, therefore minimizing the lithography-introduced contaminations. Fig. 3 shows a series of steps to produce an in-plane MoS_2 array with a pre-set pattern using IDSS. Specifically, Fig. 3(a) displays the software interface for designing droplet patterns and an OM image of as-printed DI water droplets on a SiO_2 substrate. This representative DI water droplet pattern has a pixel-to-pixel period of 500 μm, which exactly follows the period of the designed pattern. After drying of the droplets, the substrate is subsequently delivered to a CVD tube to perform the site-selective growth of MoS_2. Fig. 3(b) shows an in-plane MoS_2 array pattern produced after the CVD process. Such a MoS_2 array exhibits the same period as that of the pre-designed droplet pattern.

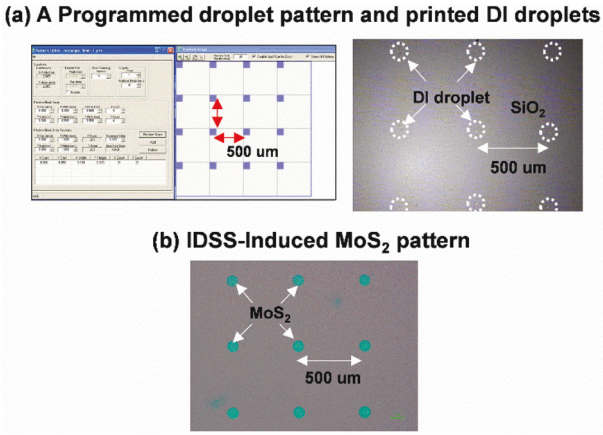

Fig. 3 Programmable droplet pattern using inkjet printing: (a) a representative droplet pattern programmed by inkjet printing and the printed corresponding DI droplet pattern; (b) an in-plane MoS_2 pattern produced by IDSS process, which exhibits the same period of that of the printed DI droplet pattern.

Fig. 4 shows the optical micrographs (OMs) of several representative arrays of in-plane MoS_2 pixel features produced by IDSS processes. In this process, DI water was used as the dispensed material for inducing site-selective growth of in-plane MoS_2. Fig. 4(a), (b), (c) and (d) display as-grown MoS_2 feature arrays with various periods (or pixel-to-pixel spacings) of 200, 350, 500 and 650 μm, respectively. Such well-defined MoS_2 feature patterns are generated with no need of any extra resist-based lithography or chemical/plasma-based etching processes. Furthermore, Fig. 4(e) shows an IDSS-produced MoS_2 pixel pattern, which forms an alphabetical character 'M'. This shows that IDSS can generate arbitrary array patterns of MoS_2 pixels. Fig. 4(f) displays the zoomed OM of a representative MoS_2 pixel in the pattern array, which has an average diameter of ~90 μm. Such a MoS_2 pixel exhibits a smooth and round boundary, which is faithfully consistent with the area profile of the inkjet-deposited droplet, and there are no MoS_2 domains observed around the pixel. This indicates that the dispensed DI droplets can induce a high selectivity for MoS_2 growth on the substrate.

To further evaluate the growth selectivity of IDSS processes, we further performed Raman and atomic force microscopy (AFM) characterizations for IDSS-produced in-plane MoS_2 pixel

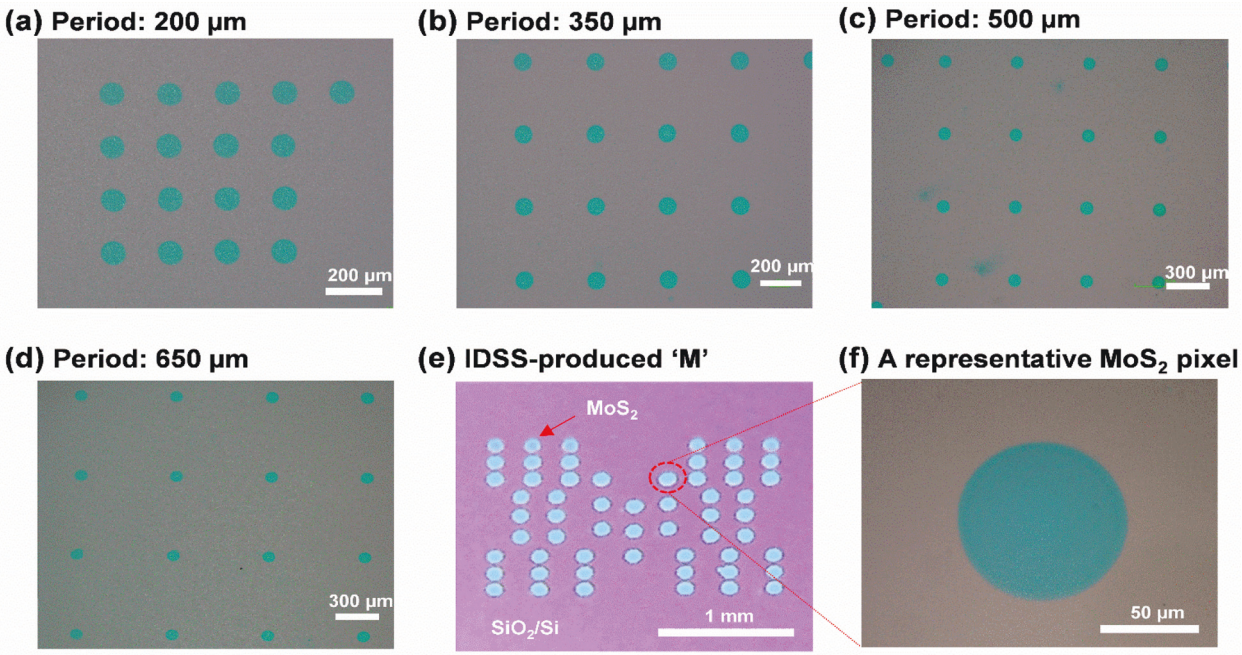

Fig. 4 Optical micrographs of IDSS-produced in-plane MoS_2 pixel features with various periods of (a) 200 μm, (b) 350 μm, (c) 500 μm, and (d) 650 μm; (e) optical micrograph of an IDSS-produced MoS_2 pixel pattern forming an alphabetical character 'M'; (f) zoomed optical micrograph of a representative MoS_2 pixel in the array, exhibiting the pixel diameter of ~90 μm.

features. Fig. 5(a) shows the Raman spectrum analyzed from the central spot of a representative MoS_2 pixel. This spectrum clearly exhibits two characteristic peaks of MoS_2, which are E^1_{2g} and A_{1g} observed at ~383 and ~407 cm^{-1}, respectively. Fig. 5(b) plots 16 Raman spectra captured from the 16 MoS_2 pixels in an array. All of these Raman spectrum curves exhibit very similar line shapes, and their E^1_{2g} and A_{1g} characteristic peaks are observed at almost the same positions. This implies a good uniformity of IDSS-produced MoS_2 pixel features. Here, the specific peak spacing between E^1_{2g} and A_{1g} peaks is measured to be ~24 cm^{-1}, which typically indicates the formation of few-layer MoS_2 with a thickness corresponding to 4–5 layers.[24–26] Fig. 5(c) further shows the spatial mappings of the E^1_{2g} and A_{1g} characteristic peaks measured over a representative MoS_2 pixel, which are labelled with red and green colors, respectively. As shown in Fig. 5(c), both E^1_{2g} and A_{1g} Raman features only appear within the pixel area previously covered with the liquid droplet, and there is no detectable E^1_{2g} or A_{1g} features outside the pixel region. Such a high spatial contrast of Raman feature distribution further verifies the high growth selectivity of IDSS. To precisely quantify the thickness of IDSS-produced in-plane MoS_2 pixels, a substrate bearing MoS_2 pixels was mechanically agitated in a sonication bath to intentionally induce partial delamination for some MoS_2 pixel layers, as shown in Fig. 5(d). Fig. 5(e) shows the AFM topography image captured over the broken edge of a representative in-plane MoS_2 pixel, which is denoted with a dashed line (*i.e.*, Line 'a') in Fig. 5(d). Fig. 5(f) also plots the scanline along Line "a", which shows an average MoS_2 thickness of ~3.48 nm, which is consistent with the average thickness value (*i.e.*, 4–5 layers) estimated from Raman results.

To evaluate the electronic properties of IDSS-produced in-plane MoS_2 features, an array of field effect transistors (FETs) based on such MoS_2 pixel features were fabricated and characterized. Fig. 6(a) shows the optical microscopy (OM) image of an array of FETs made on a set of IDSS-produced in-plane MoS_2 pixels. For each FET, the channel length and average channel width are 2 and 50 μm, respectively. Additional information about the FET fabrication is described in the Methods and Materials section. Fig. 6(b) displays the transfer characteristic curve acquired by measuring a representative MoS_2 FET, which is plotted in linear (black) and semi-logarithmic (red) scales. A typical n-type transport behavior is shown from the FET. Under the given measurement condition (V_{ds} = 3 V, V_g = −40 to 40 V), the FET exhibits on–off switching ratio larger than 10^4 and field-effect mobility of ~0.15 $cm^2\ V^{-1}\ s^{-1}$, respectively. The transfer characteristic curves measured from all 16 MoS_2 FETs in the same array are plotted in Fig. S2.† The field-

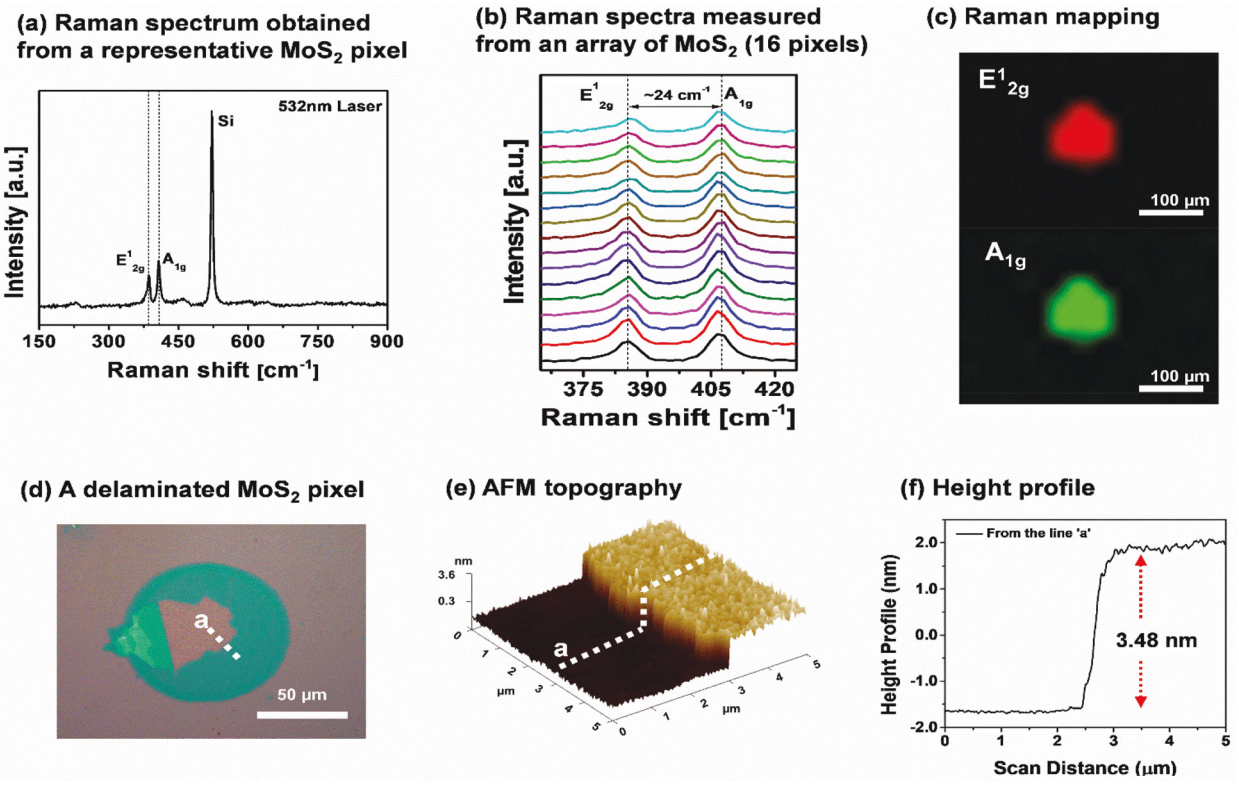

Fig. 5 Characterizations of IDSS-produced in-plane MoS_2 pixel features: (a) Raman spectrum measured from the central region of a representative MoS_2 pixel; (b) 16 Raman spectra with their E^1_{2g} and A_{1g} characteristic peaks, obtained from the 16 MoS_2 pixels in an array; (c) spatial Raman mappings of the E^1_{2g} and A_{1g} characteristic peaks measured over a representative MoS_2 pixel. (d) Optical micrograph of a representative in-plane MoS_2 pixel with induced partial delamination for AFM measurement; (e) AFM topography image captured over a broken edge of a representative in-plane MoS_2 pixel; (f) AFM scanline along Line "a" of a few-layer MoS_2 pixel.

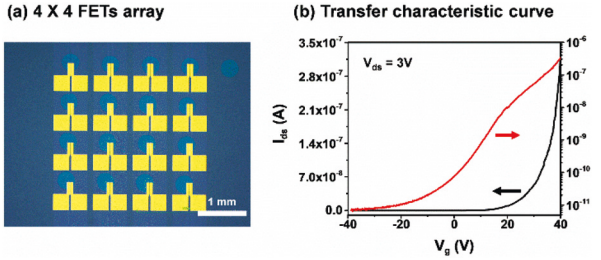

Fig. 6 Measurement of electronic properties of IDSS-produced in-plane MoS_2 features: (a) optical micrograph of an array of FETs fabricated on a set of IDSS-produced in-plane MoS_2 pixels (channel length: 2 μm, channel width: 50 μm, source/drain contacts: 50 nm-thick Au with a 5 nm-thick Ti adhesion layer); (b) a transfer characteristic curve obtained from a representative MoS_2 FET, which is plotted in linear (black) and semi-logarithmic (red) scales.

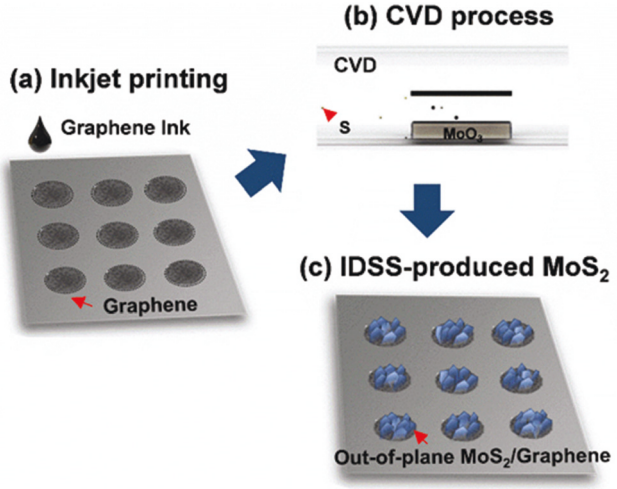

Fig. 7 Schematic diagram of IDSS process using graphene ink solution to produce out-of-plane MoS_2: (a) inkjet printing of graphene ink solution droplets at designated locations on the SiO_2/Si substrate. (b) CVD process to induce site-selective growth of MoS_2 within the printed droplet patterns. (c) Out-of-plane MoS_2 array produced by IDSS process using the graphene ink.

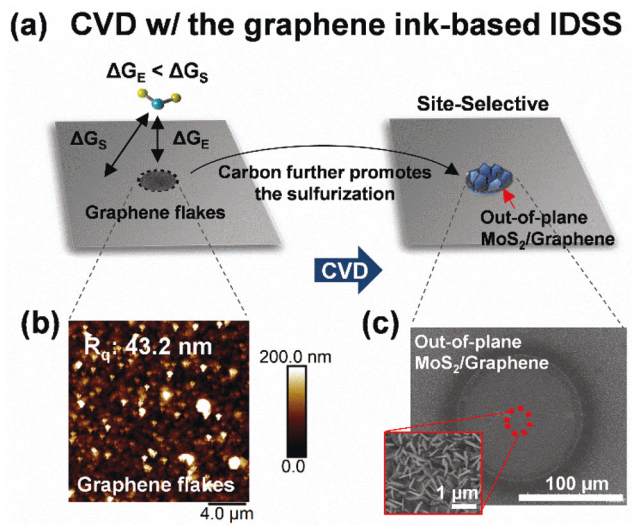

Fig. 8 Growth of out-of-plane MoS_2 with the IDSS by using graphene ink: (a) schematic illustration of the site-selective nucleation of out-of-plane MoS_2 with the graphene ink-based IDSS; (b) AFM image of a SiO_2/Si substrate area ever covered by inkjet-dispensed graphene ink droplet; (c) SEM images of IDSS-produced out-of-plane MoS_2/graphene pixel.

effect mobility values measured from these FETs are comparable to those of recently reported FETs fabricated by using the as-grown MoS_2 flakes grown by CVD and other site-selective approaches.[24,27,28]

To leverage IDSS-produced MoS_2 structures for electrochemical applications such as catalyst and lithium-ion battery (LIB), it is highly desirable to explore the applicability about using IDSS to generate MoS_2 structures rich of out-of-plane edges.[29,30] In this work, we further explore the IDSS processing conditions capable of generating MoS_2 pixel features rich of out-of-plane edges, which could be used as the anode structures for LIBs. After testing different inkjet-dispensed liquid droplets in IDSS processes, we found that droplets of graphene ink solution on a SiO_2/Si substrate can lead to a high yield of out-of-plane MoS_2 structures during CVD. Such out-of-plane MoS_2 structures are expected to provide much more accessible pathways for sustaining lithiation processes in comparison with in-plane MoS_2 structures.[31,32] Fig. 7 schematically illustrates the IDSS process to produce out-of-plane MoS_2 features, whose 2D crystal grains are not parallel to the horizontal substrate surface. In this IDSS process, graphene ink solution, instead of DI water, is dispensed as droplets on the target substrate, as illustrated in Fig. 7(a). Graphene ink purchased from Sigma Aldrich is manufactured by mixing graphene particles with cyclohexanone/terpineol solution (2.4 wt% of graphene). The graphene ink solution has a viscosity of 10 mPa s at 30 °C, and the average graphene particles size is less than 3 μm. Fig. 7(b) and (c), respectively, illustrate the CVD process for the site-selective formation of MoS_2 structures and as-produced out-of-plane MoS_2 pixels.

Fig. 8 shows analysis of the possible mechanism responsible for site-selective growth of out-of-plane MoS_2 features. As illustrated in Fig. 8(a), after the solvent of dispensed graphene ink solution completely evaporates, graphene flakes are left on the substrate and increase local surface roughness. In comparison with the residues deposited from DI water, such graphene flakes are expected to form more step edges, around which the nucleation barrier energy is lower than that in the smooth areas. Such lower nucleation barrier energy at step edges (ΔG_E) leads to site-selective nucleation of MoS_2 on the specific spots with graphene flakes. In addition, the carbon contained in graphene flakes could significantly promote the reduction of MoO_3 precursors, which forms MoO_{3-x} ($x > 1$) at a high rate. Such a high rate formation of MoO_{3-x} ($x > 1$) continuously consumes sulfur vapor for the chemical conversion process (or sulfurization process), which effectively limits the diffusion of sulfur vapor along the in-plane MoS_2 layer direction. Such a localized and limited diffusion of sulfur vapor

results in the formation of out-of-plane MoS_2 features.[18,33] Experimental findings shown in Fig. 8(b) and (c) support the above speculation. Specifically, Fig. 8(b) shows the AFM topography image of a substrate area ever covered by an inkjet-dispensed graphene ink droplet. The surface roughness (R_q) of this area is measured to be ~43.2 nm, which is ~166 times and ~9 times larger than those of the control (or surroundings) and DI-water-deposited substrate areas, respectively. Such a large surface roughness is due to the graphene flakes left within the droplet-covered spot after drying of the graphene ink droplets. Fig. 8(c) shows the SEM images of an IDSS-produced out-of-plane MoS_2 pixel feature on top of the inkjet-dispensed graphene flakes.

Fig. 9(a) shows the optical micrographs of an array of as-dispensed graphene ink droplets (pixel diameter ~90 μm; pixel-to-pixel spacing ~200 μm). To demonstrate inkjet dispensing of graphene ink droplets with various sizes, a relatively large graphene ink droplet (pixel diameter ~1 mm) was dispensed and also shown in Fig. 9(a). After the subsequent CVD process, out-of-plane MoS_2 structures are selectively synthesized on top of the inkjet-dispensed graphene pixel features. Fig. 9(b) shows the scanning electron micrographs (SEMs) of as-grown MoS_2/graphene pixel arrays with the period of 500 μm and 200 μm. The magnified SEM image in Fig. 9(b) clearly shows that such a pixel feature is dominantly composed of out-of-plane MoS_2 flakes, which are randomly arranged along various out-of-plane orientations. Fig. 9(c) shows the Raman spectrum measured from a representative out-of-plane MoS_2/graphene pixel. Two characteristic peaks (E^1_{2g} and A_{1g}) of MoS_2 are observed at ~381 and ~407 cm^{-1}, respectively. The Raman intensity ratio between in-plane Mo–S phonon mode (E^1_{2g}) and out-of-plane Mo–S phonon mode (A_{1g}) peaks is 1 : 3, which also strongly implies the abundance of out-of-plane MoS_2 flakes in the pixel.[34] Furthermore, characteristic Raman peaks (D, G, and 2D) of graphene are also observed at the larger Raman shifts. The G and 2D peaks, appearing at ~1581 and ~2711 cm^{-1}, are associated with the E_{2g} phonon vibration mode at the center of the Brillouin zone and the second order of the D peak, respectively.[35,36] Notably, the D peak at ~1353 cm^{-1} is attributed to the breathing mode of sp^2 carbon rings and activated by the existence of disorders in graphene edges or defects within graphene flakes.[37] To further reveal the type of defects responsible for the D peak, the Raman spectra, measured from six different graphene ink droplets dispensed and dried on a SiO_2/Si substrate, were acquired and analyzed. Fig. S3(a)–(e)† show the Raman spectra obtained from representative pixel locations with inkjet-dispensed and subsequently dried graphene ink droplets. From such Raman spectra, the intensity ratios between D and G peaks (I_D/I_G) and the full-width half-maximum values of the G peaks (FWHM (G)) were extracted. Fig. S3(f)† plots the I_D/I_G data as a function of FWHM(G) values and shows that the I_D/I_G values (~0.4) are quite independent of FWHM(G) values. For the graphene flakes rich in in-plane defects, it is expected that a higher I_D/I_G value is usually correlated with a larger FWHM(G) value.[37] Therefore, our Raman results imply that the D peaks observed

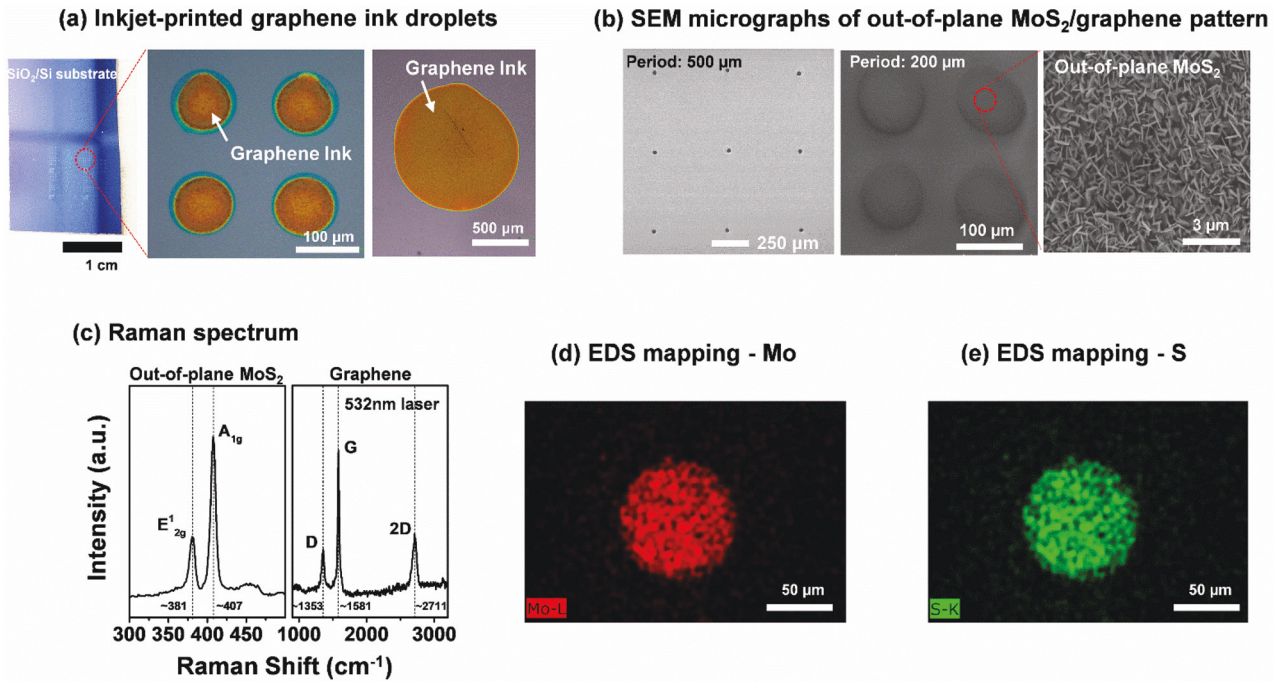

Fig. 9 Characterizations of IDSS-produced out-of-plane MoS_2 pixel features: (a) optical micrographs of as-dispensed graphene ink droplets; (b) SEM images of as-grown out-of-plane MoS_2/graphene with different period of 200 and 500 μm; (c) Raman spectrum from a representative out-of-plane MoS_2/graphene pixel, which exhibits characteristic peaks of both MoS_2 (E^1_{2g} and A_{1g}) and graphene (D, G, and 2D); (d) and (e) show the EDS mapping images of the spatial distribution of Mo and S atoms around an out-of-plane MoS_2/graphene pixel.

in our inkjet-deposited graphene flakes dominantly originate from the disorders along graphene edges. Such an analysis conclusion is also consistent with the fact that graphene ink consists of lots of submicrometer flakes that, after dispensed, stack together and form abundantly exposed edges.[38] Such graphene structures provide a large number of out-of-plane edge sites, which are expected to serve as effective seeding promoters for inducing site-selective nucleation of out-of-plane MoS_2 grains.[18] Fig. 9(d) and (e) show the energy-dispersive X-ray spectroscopy (EDS) mapping images for displaying the spatial distributions of Mo and S atoms around a MoS_2/graphene pixel. Such EDS results show that Mo/S signals are highly localized within the pixel feature area, and therefore IDSS can also result in a high site selectivity for growing out-of-plane MoS_2 structures.

To evaluate the electrochemical properties of IDSS-produced out-of-plane MoS_2/graphene structures, we performed a half-cell battery test. Fig. 10(a) schematically illustrates the test setup of the cell, in which an out-of-plane MoS_2/graphene pixel serves as the electrode component. To make such a half-cell battery, graphene ink droplets with average footprint diameter of ~1 mm are dispensed on a SiO_2 substrate by inkjet printing, and then an IDSS process is conducted to produce out-of-plane MoS_2/graphene pixel features. Such pixel features also have an average footprint diameter of ~1 mm, which can result in charge–discharge characteristic current signals measurable for our current battery characterization tool. The smaller MoS_2/graphene pixel features could be used for making batteries if the characterization tools with improved measurement limits are implemented. However, our current ~1 mm size MoS_2/graphene pixel features are already small enough for on-chip battery applications. After the IDSS process, a 100 nm-thick Ti, which does not react with the electrolyte, is deposited as an external electrode. Inside an argon glovebox, a celgard 2025 trilayer separator is placed on top of the MoS_2/graphene pixel and soaked with electrolyte (1 M Lithium hexafluorophosphate, $LiPF_6$ in 1 : 1 EC : EMC, ethylene carbonate : ethylmethyl carbonate). The out-of-plane MoS_2 and graphene flakes in the pixel serve as the cathode and the current collector, respectively. A Li metal foil placed on top of the separator is used as the counter electrode (anode). A tungsten probe is used to contact the titanium current collector, and a pogo-pin is used to contact the Li electrode.

Fig. 10(b) shows the lithiation (discharge) and delithiation (charge) profiles of MoS_2/graphene electrode *vs.* Li/Li^+. The test was carried out in the sweep voltage range of 0.05–3 V at a constant current density of 55 μA cm^{-2}. On the 1st discharge curve, the plateau appearing at 1.1 V is attributed to Li intercalation into MoS_2 layers and formation of Li_xMoS_2 ($0 \le x \le 4$). Another plateau at 0.6 V on the same curve is attributed to the conversion reaction, which is described by $MoS_2 + 2xLi^+ + 2xe^- \rightarrow Mo + xLi_2S$. The plateau in the voltage regime lower than 0.2 V is attributed to the lithiation of graphene, which could form LiC_x ($0 \le x \le 6$). In the 2nd and 3rd discharge profiles, the plateau at 1.1 V disappears because of the irreversibility of conversion reaction. On the other hand, during three times charging processes, all profiles display one plateau at 2.3 V, which indicates delithiation of Li_2S and generation of S. Areal capacities of the first discharge and charge are evaluated to be 206 μA h cm^{-2} and 113 μA h cm^{-2}, respectively. Considering the similar current density (50 μA cm^{-2}) set in the study by He *et al.*, areal discharge capacity obtained from our mini-size LIB is estimated to be comparable to that measured from R2032 type coin cells (~180 μA h cm^{-2}).[30] During the first charge/discharge cycle, coulombic efficiency (CE) is initially low (~55%), which could be ascribed to the electrolyte decomposition or irreversible reaction processes.[30] However, CE increases to 80% and 84% in the 2nd and 3rd cycles, respectively, and it is expected to further rise with increasing the number of cycles, as reported in the previous studies.[30,39,40] This result suggests that IDSS-produced MoS_2/graphene pixel structures can be used for making miniaturized on-chip battery electrodes with good lithium storage properties.

To further analyze the electrochemical reaction properties of IDSS-produced MoS_2/graphene electrodes, cyclic voltammograms (CVs) of the half-cell battery were measured in the voltage range of 0.05–3 V at a constant scan rate of 0.5 mV s^{-1} and plotted in Fig. 10(c). The CV curve in the first cathodic sweep shows two peaks at 1.1 V and 0.6 V, which indicate the intercalation and conversion reactions, respectively. In the fol-

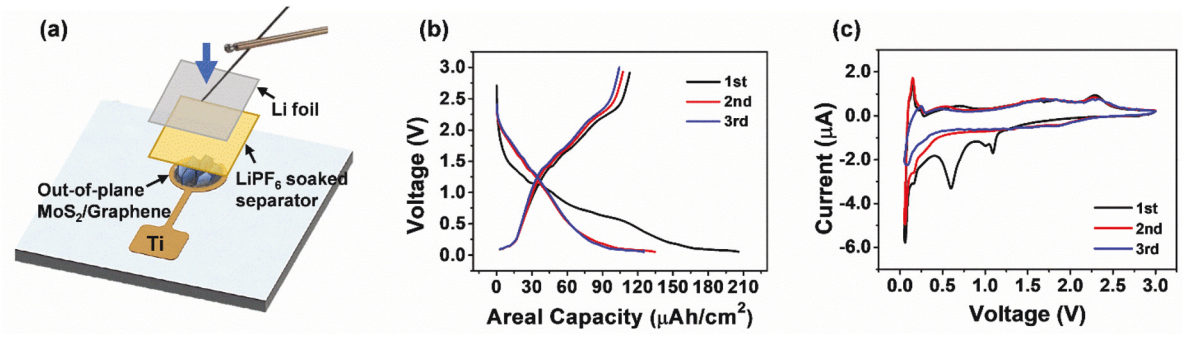

Fig. 10 Measurement of electrochemical properties of IDSS-produced out-of-plane MoS_2/graphene pixel electrode: (a) schematic illustration of the half-cell Li-ion battery test setup; (b) discharge/charge profiles of MoS_2/graphene electrode measured in 0.05–3 V at 55 μA cm^{-2} current density; (c) cyclic voltammograms obtained from a MoS_2/graphene pixel electrode in the range of 0.05–3 V at the 0.5 mV s^{-1} scan rate.

lowing cathodic scans, these two peaks at 1.1 V and 0.6 V disappear as a result of the irreversible conversion reaction, whereas a small peak emerges at ~1.8 V arising from the Li_2S formation.[40–42] In the anodic sweeps, the peak at 1.7 V is attributed to the removal of Li^+ ions pertaining to the Mo reduction,[39,43] and the peak at 2.3 V is associated with the oxidation of Li_2S to form S. Additionally, during the discharge/charge process, the peaks at ~0.2 V shows the lithiation/delithiation of graphene features.[39,44] All potential peak locations are well consistent with the plateau voltages acquired in the charge/discharge characterizations. Additional characterization results about the electrochemical impedance of the out-of-plane MoS_2/graphene electrodes are presented in Fig. S4 in the ESI.†

3. Conclusions

In this study, we developed an IDSS method, which enables scalable fabrication of MoS_2 structures at designated locations on a chip substrate without requiring additional lithography and etching processes. In the IDSS process, inkjet-dispensed microscale liquid droplets (*i.e.*, DI water or graphene ink) first predefine the target locations on a substrate and in-plane or out-of-plane MoS_2 structures are subsequently synthesized at the defined locations on the substrate during the site-selective CVD process. We attributed such selective growth capability of IDSS to local topography change within droplet-covered regions, which lowers the nucleation barrier energy and serves as effective nucleation seeds during the CVD process. Especially, as well as the site-selective capability, IDSS can also be a facile and controllable method to produce MoS_2 exhibiting different structures. By depositing DI water droplets during the IDSS process, in-plane MoS_2 features are dominantly synthesized at defined locations. Such in-plane MoS_2 features fabricated into an array of the working transistors exhibit a good uniformity in their transfer characteristics. Furthermore, graphene ink droplets applied during the IDSS process dominantly induce out-of-plane MoS_2 features selectively synthesized on top of inkjet-printed graphene flakes. Such a hierarchical structure of out-of-plane MoS_2/graphene was fabricated and demonstrated into a miniaturized lithium-ion battery electrode structure, which exhibits appealing electrochemical characteristics because of abundant edges in the out-of-plane MoS_2 in combination with efficient charge collecting and delivering by the graphene. The IDSS method could be a promising cost-efficient scalable nanomanufacturing technique, which can pave the way to the development of a new generation miniaturized on-chip energy storage devices.

In future follow-up studies, not only DI water and graphene ink used in this study but also a wide variety of base printing materials could be exploited, therefore expanding the application scope of the IDSS method. For example, liquid metals such as gallium (Ga), liquid gallium-indium alloy (EGaIn), and Galinstan can be dispensed by the inkjet systems with programmed patterns.[45,46] The low melting temperatures of such liquid metals (typically lower than 30 °C) can enable simple and easy patterning of metallic sources with no need of complicated pre-processes. The dispensed liquid metals could serve as effective nucleation seeds due to the low nucleation barrier energy at their step edges, and they could be also exploited as effective metal dopants during CVD processes. Such a promising doping function of the liquid metals is anticipated to open up new applications of the IDSS method, especially in the device fields that demand bandgap engineering techniques.

4. Materials and methods

Printing of droplet patterns

First, SiO_2/Si substrates are cleaned with Aceton and IPA solution under sonication for 5 minutes each and cleaned with piranha solution for 10 minutes. For growing the in-plane MoS_2 structures, droplet patterns of deionized water are printed on the substrate using inkjet printer (Dimatix MP-2831, Fujifilm) while the substrate is heated to 55 °C. Due to the very small volume (~10 pL), droplets are evaporated quickly before the sample being loaded into quartz tube for the following CVD process. To grow the out-of-plane MoS_2 structures, graphene ink (793 663–5 mL, Sigma Aldrich) is printed with the same printer while the substrate temperature is 25 °C. Subsequently, droplets of graphene ink on SiO_2/Si are cured at 300 °C for 25 minutes in Ar atmosphere.

Chemical vapor deposition (CVD) process

During a CVD step, sulfur (S, 150 mg, 99.5%, Sigma Aldrich) and molybdenum trioxide (MoO_3, 10 mg, 99.97%, Sigma Aldrich) are added at the upstream and center of a 1″-Dia. quartz tube, respectively. The SiO_2/Si substrates with printed patterns prepared in the previous step are loaded and flipped over above the MoO_3 source. To deliver precursor molecules during MoS_2 synthesis, we used inert Ar gas (99.999%, Cryogenic Gases). The delivery rate of the Ar is optimized to 150 sccm. The furnace chamber is heated up to 800 °C and maintained for 3 min to induce sufficient nucleation of MoS_2. Afterwards, the furnace is naturally cooled down to the room temperature, and the substrates with IDSS-grown MoS_2 patterns are retrieved from the quartz tube.

Fabrication and characterization of FETs

The back-gate FETs are fabricated on IDSS-produced in-plane MoS_2 pixels. Two metal contacts with thickness of 5 nm Ti/50 nm Au are photolithographically patterned and deposited. Characteristic curves of FETs are measured using a Keithley 4200 semiconductor parameter analyzer.

Fabrication and characterization of on-chip battery

To fabricate the on-chip battery with IDSS-produced out-of-plane MoS_2/graphene pixels, C-shaped metallic pads (100 nm Ti) are deposited through the aligned polyimide shadow mask. Cells are prepared in the Ar-filled glove box, where the oxygen

and H_2O levels are controlled below 0.5 ppm. MoS_2/graphene pixel and Li foil are used as the cathode and counter electrode respectively, and 1 M $LiPF_6$ in a (1 : 1 volume ratio) mixture of ethylene carbonate (EC)/ethyl methyl carbonate (EMC) is used as electrolyte. A trilayer porouse separator (Celgard 2025) was used to prevent electrical contact between the Li metal and the MoS_2. The electrochemical property of on-chip battery is measured using potentiostat (Biologic, SP-200) and the lab-made probe setup. Charge/discharge of the cell is tested in the 0.05–3 V voltage window at 55 μA cm^{-2} current density for 3 cycles each. Cyclic voltammogram (CV) measurement is performed at a scan rate of 0.5 mV s^{-1} in the same voltage range. Impedance plot is obtained in the frequency of 0.5 Hz–1 MHz by applying 5 mV amplitude AC voltage, and EC-lab software is used to fit the impedance spectra to the equivalent circuit model.

Conflicts of interest

There are no conflicts to declare.

Acknowledgements

The inkjet printing work is supported by NSF grant # CMMI-1636132, the device fabrication work is supported by NSF grant # ECCS-1708706. N.P.D. acknowledges supported by NSF Grant # 1727918. The authors would like to thank the staff of the University of Michigan Lurie Nanofabrication Facility for providing the support of AFM imaging and device fabrication.

References

1 W. Zheng, Y. Xu, L. Zheng, C. Yang, N. Pinna, X. Liu and J. Zhang, *Adv. Funct. Mater.*, 2020, 2000435.
2 G. Eda, H. Yamaguchi, D. Voiry, T. Fujita, M. Chen and M. Chhowalla, *Nano Lett.*, 2011, **11**, 5111–5116.
3 K. Andrews, A. Bowman, U. Rijal, P.-Y. Chen and Z. Zhou, *ACS Nano*, 2020, **14**(5), 6232–6241.
4 B. Ryu, E. Yang, Y. Park, K. Kurabayashi and X. Liang, *J. Vac. Sci. Technol., B: Nanotechnol. Microelectron.: Mater., Process., Meas., Phenom.*, 2017, **35**, 06G805.
5 G. A. Salvatore, N. Münzenrieder, C. Barraud, L. Petti, C. Zysset, L. Büthe, K. Ensslin and G. Tröster, *ACS Nano*, 2013, **7**, 8809–8815.
6 H. Nam, S. Wi, H. Rokni, M. Chen, G. Priessnitz, W. Lu and X. Liang, *ACS Nano*, 2013, **7**, 5870–5881.
7 G. R. Bhimanapati, T. Hankins, Y. Lei, R. A. Vilá, I. Fuller, M. Terrones and J. A. Robinson, *ACS Appl. Mater. Interfaces*, 2016, **8**, 22190–22195.
8 R. Addou, S. McDonnell, D. Barrera, Z. Guo, A. Azcatl, J. Wang, H. Zhu, C. L. Hinkle, M. Quevedo-Lopez and H. N. Alshareef, *ACS Nano*, 2015, **9**, 9124–9133.
9 M. Amani, M. L. Chin, A. L. Mazzoni, R. A. Burke, S. Najmaei, P. M. Ajayan, J. Lou and M. Dubey, *Appl. Phys. Lett.*, 2014, **104**, 203506.
10 R. Ionescu, A. George, I. Ruiz, Z. Favors, Z. Mutlu, C. Liu, K. Ahmed, R. Wu, J. S. Jeong and L. Zavala, *Chem. Commun.*, 2014, **50**, 11226–11229.
11 J. Jadwiszczak, C. O'Callaghan, Y. Zhou, D. S. Fox, E. Weitz, D. Keane, C. P. Cullen, I. O'Reilly, C. Downing and A. Shmeliov, *Sci. Adv.*, 2018, **4**, eaao5031.
12 S. Y. Yang, J. G. Oh, D. Y. Jung, H. Choi, C. H. Yu, J. Shin, C. G. Choi, B. J. Cho and S. Y. Choi, *Small*, 2015, **11**, 175–181.
13 J. Zhao, H. Yu, W. Chen, R. Yang, J. Zhu, M. Liao, D. Shi and G. Zhang, *ACS Appl. Mater. Interfaces*, 2016, **8**, 16546–16550.
14 Y. Liu, H. Nan, X. Wu, W. Pan, W. Wang, J. Bai, W. Zhao, L. Sun, X. Wang and Z. Ni, *ACS Nano*, 2013, **7**, 4202–4209.
15 S. Najmaei, Z. Liu, W. Zhou, X. Zou, G. Shi, S. Lei, B. I. Yakobson, J.-C. Idrobo, P. M. Ajayan and J. Lou, *Nat. Mater.*, 2013, **12**, 754–759.
16 G. H. Han, N. J. Kybert, C. H. Naylor, B. S. Lee, J. Ping, J. H. Park, J. Kang, S. Y. Lee, Y. H. Lee and R. Agarwal, *Nat. Commun.*, 2015, **6**, 6128.
17 A. Teichler, J. Perelaer and U. S. Schubert, *J. Mater. Chem. C*, 2013, **1**, 1910–1925.
18 Y. Shi, H. Li, J. I. Wong, X. Zhang, Y. Wang, H. Song and H. Y. Yang, *Sci. Rep.*, 2015, **5**, 10378.
19 I. V. Markov, *Crystal growth for beginners: fundamentals of nucleation*, crystal growth and epitaxy, World scientific, 2003.
20 J. Gao, J. Yip, J. Zhao, B. I. Yakobson and F. Ding, *J. Am. Chem. Soc.*, 2011, **133**, 5009–5015.
21 B. M. Stewart, *Lab. Med.*, 2000, **31**, 605–612.
22 *Laboratory Water: Its Importance and Application*, NIH, 2013, https://www.orf.od.nih.gov/TechnicalResources/Documents/DTR%20White%20Papers/Laboratory%20Water-Its%20Importance%20and%20Application-March-2013_508.pdf.
23 G. H. Han, F. Gunes, J. J. Bae, E. S. Kim, S. J. Chae, H.-J. Shin, J.-Y. Choi, D. Pribat and Y. H. Lee, *Nano Lett.*, 2011, **11**, 4144–4148.
24 B. Ryu, D. Li, C. Park, H. Rokni, W. Lu and X. Liang, *ACS Appl. Mater. Interfaces*, 2018, **10**, 43774–43784.
25 H. Li, Q. Zhang, C. C. R. Yap, B. K. Tay, T. H. T. Edwin, A. Olivier and D. Baillargeat, *Adv. Funct. Mater.*, 2012, **22**, 1385–1390.
26 M. Boukhicha, M. Calandra, M.-A. Measson, O. Lancry and A. Shukla, *Phys. Rev. B: Condens. Matter Mater. Phys.*, 2013, **87**, 195316.
27 H. J. Kim, H. Kim, S. Yang and J. Y. Kwon, *Small*, 2017, **13**, 1702256.
28 X. Chen, Y. J. Park, T. Das, H. Jang, J.-B. Lee and J.-H. Ahn, *Nanoscale*, 2016, **8**, 15181–15188.
29 T. Stephenson, Z. Li, B. Olsen and D. Mitlin, *Energy Environ. Sci.*, 2014, **7**, 209–231.
30 J. He, C. Zhang, H. Du, S. Zhang, P. Hu, Z. Zhang, Y. Ma, C. Huang and G. Cui, *Electrochim. Acta*, 2015, **178**, 476–483.

31 G. Wang, J. Zhang, S. Yang, F. Wang, X. Zhuang, K. Müllen and X. Feng, *Adv. Energy Mater.*, 2018, **8**, 1702254.
32 Y. Teng, H. Zhao, Z. Zhang, Z. Li, Q. Xia, Y. Zhang, L. Zhao, X. Du, Z. Du and P. Lv, *ACS Nano*, 2016, **10**, 8526–8535.
33 D. Kong, H. Wang, J. J. Cha, M. Pasta, K. J. Koski, J. Yao and Y. Cui, *Nano Lett.*, 2013, **13**, 1341–1347.
34 V. Shokhen, Y. Miroshnikov, G. Gershinsky, N. Gotlib, C. Stern, D. Naveh and D. Zitoun, *Sci. Rep.*, 2017, **7**, 3280.
35 L. G. Cançado, A. Jorio, E. M. Ferreira, F. Stavale, C. A. Achete, R. B. Capaz, M. V. d. O. Moutinho, A. Lombardo, T. Kulmala and A. C. Ferrari, *Nano Lett.*, 2011, **11**, 3190–3196.
36 A. C. Ferrari, J. Meyer, V. Scardaci, C. Casiraghi, M. Lazzeri, F. Mauri, S. Piscanec, D. Jiang, K. Novoselov and S. Roth, *Phys. Rev. Lett.*, 2006, **97**, 187401.
37 F. Torrisi, T. Hasan, W. Wu, Z. Sun, A. Lombardo, T. S. Kulmala, G.-W. Hsieh, S. Jung, F. Bonaccorso and P. J. Paul, *ACS Nano*, 2012, **6**, 2992–3006.
38 S. Majee, C. Liu, B. Wu, S.-L. Zhang and Z.-B. Zhang, *Carbon*, 2017, **114**, 77–83.
39 K. Rana, J. Singh, J.-T. Lee, J. H. Park and J.-H. Ahn, *ACS Appl. Mater. Interfaces*, 2014, **6**, 11158–11166.
40 L. Oakes, R. Carter, T. Hanken, A. P. Cohn, K. Share, B. Schmidt and C. L. Pint, *Nat. Commun.*, 2016, **7**, 11796.
41 L. Zhang, D. Sun, J. Kang, J. Feng, H. A. Bechtel, L.-W. Wang, E. J. Cairns and J. Guo, *Nano Lett.*, 2018, **18**, 1466–1475.
42 S. Ding, D. Zhang, J. S. Chen and X. W. D. Lou, *Nanoscale*, 2012, **4**, 95–98.
43 J. Xiao, X. Wang, X. Q. Yang, S. Xun, G. Liu, P. K. Koech, J. Liu and J. P. Lemmon, *Adv. Funct. Mater.*, 2011, **21**, 2840–2846.
44 A. P. Cohn, L. Oakes, R. Carter, S. Chatterjee, A. S. Westover, K. Share and C. L. Pint, *Nanoscale*, 2014, **6**, 4669–4675.
45 M. B. Ghasemian, M. Mayyas, S. A. Idrus–Saidi, M. A. Jamal, J. Yang, S. S. Mofarah, E. Adabifiroozjaei, J. Tang, N. Syed and A. P. O'Mullane, *Adv. Funct. Mater.*, 2019, **29**, 1901649.
46 A. Zavabeti, B. Y. Zhang, I. A. de Castro, J. Z. Ou, B. J. Carey, M. Mohiuddin, R. Datta, C. Xu, A. P. Mouritz and C. F. McConville, *Adv. Funct. Mater.*, 2018, **28**, 1804057.